

# Optically and Structurally Stabilized Plasmo-Bio Interlinking Networks

Wei-Kuan Lin, Guangjie Cui, Zachary Burns, Xintao Zhao, Yunbo Liu, Zhijia Zhang, Yi Wang, Xingchen Ye, Younggeun Park,\* and Somin Eunice Lee\*

Visualization of dynamic interlinking networks which respond and adapt to the constantly changing environment would be highly beneficial in developing new composite materials and active/responsive materials. Here, optically and structurally stabilized plasmo-bio interlinking networks (PBINs) free from photobleaching for high resolution, long term visualization are reported. Necessary for structural and optical stability, a new stability algorithm to comprehensively quantify stability and detect minute instability undetectable by traditional methods is introduced. Biocompatible plasmonic gold nanorods (Bio-AuNRs) are synthesized for high resolution, long term imaging by utilizing bromide-free alternatives to achieve CTA+ free. Systematic physical, chemical, and biological characterizations reveal the structural and optical stability of Bio-AuNRs required for constructing PBIN. Lastly, with actin as a model of interlinking networks of the cytoskeleton, optically and structurally stable PBIN (100% CTA+ free, 97% crosslinking rate) in applications as active/responsive materials, are demonstrated.

composite materials<sup>[1–3]</sup> and active/responsive materials.<sup>[4–6]</sup> However, conventional light microscopy yields limited resolution, owing to light diffraction, for visualizing complex dynamics of interlinking networks. Recently, super-resolution microscopy techniques can overcome the diffraction limit and achieve high resolution. Methods such as stimulated emission depletion,<sup>[7]</sup> ground state depletion microscopy,<sup>[8]</sup> and reversible saturable optical fluorescence transitions<sup>[9]</sup> enhance resolution by utilizing spectral separation of fluorophores exhibiting nonlinear response to excitation. Other methods such as super-resolution optical fluctuation imaging,<sup>[10]</sup> spectral precision distance microscopy,<sup>[11]</sup> photoactivated localization microscopy,<sup>[12]</sup> and stochastic optical reconstruction microscopy<sup>[13]</sup> enhance resolution by utilizing temporal separation of fluorophores.

Interlinking networks, such as the cytoskeleton, dynamically respond and adapt to the constantly changing environment (Figure 1). Detailed visualization of the complex dynamics of interlinking networks would be highly beneficial in developing

Such super-resolution microscopy techniques rely on fluorophores susceptible to photobleaching, limiting time-resolved visualization of the complex dynamics of interlinking networks.

By contrast, plasmonic nanostructures, such as Bio-AuNRs, are not susceptible to photobleaching, making them potential candidates as super-resolution probes for dynamic interlinking networks. Owing to the collective oscillation of electron density at the metal-dielectric interface, plasmonic nanostructures exhibit strong and stable scattering, absorbance, and coupling properties based on their geometries and relative positions. Proximal plasmonic nanostructures can be spectrally or temporally isolated within interlinking networks under the condition that nanostructures maintain their plasmonic properties. Thus, three requirements must be fulfilled: 1) CTA+ free, 2) structurally stable under physical, chemical, and biological environments, and 3) efficient crosslinking with interlinking networks. In this work, we present a new method utilizing alternative bromide-free surfactants, hexadecyltrimethylammonium chloride (CTAC), to achieve 100% CTA+ free necessary for stable, efficient crosslinking. We demonstrate optically and structurally stable plasmo-bio interlinking networks (PBINs) with 97% crosslinking rate by incorporating biocompatible CTA+ free AuNRs (Bio-AuNRs). Necessary for structural and optical stability, we introduce a new stability algorithm to comprehensively quantify stability under various physical, chemical, and biological environments. This work paves the way toward super-resolution imaging of dynamic interlinking networks free of photobleaching.

W.-K. Lin, G. Cui, Z. Burns, X. Zhao, Y. Liu, Z. Zhang  
Department of Electrical and Computer Engineering  
University of Michigan  
Ann Arbor, MI 48109, USA

Y. Wang, Prof. X. Ye  
Department of Chemistry  
Indiana University  
Bloomington, IN 47405, USA

Dr. Y. Park  
Department of Mechanical Engineering  
Center for Integrative Research in Critical Care  
University of Michigan  
Ann Arbor, MI 48109, USA  
E-mail: ygpark@umich.edu

Prof. S. E. Lee  
Department of Electrical and Computer Engineering  
Department of Biomedical Engineering  
Biointerfaces Institute  
Macromolecular Science and Engineering  
University of Michigan  
Ann Arbor, MI 48109, USA  
E-mail: sleee@umich.edu

 The ORCID identification number(s) for the author(s) of this article can be found under <https://doi.org/10.1002/admi.202001370>.

DOI: 10.1002/admi.202001370

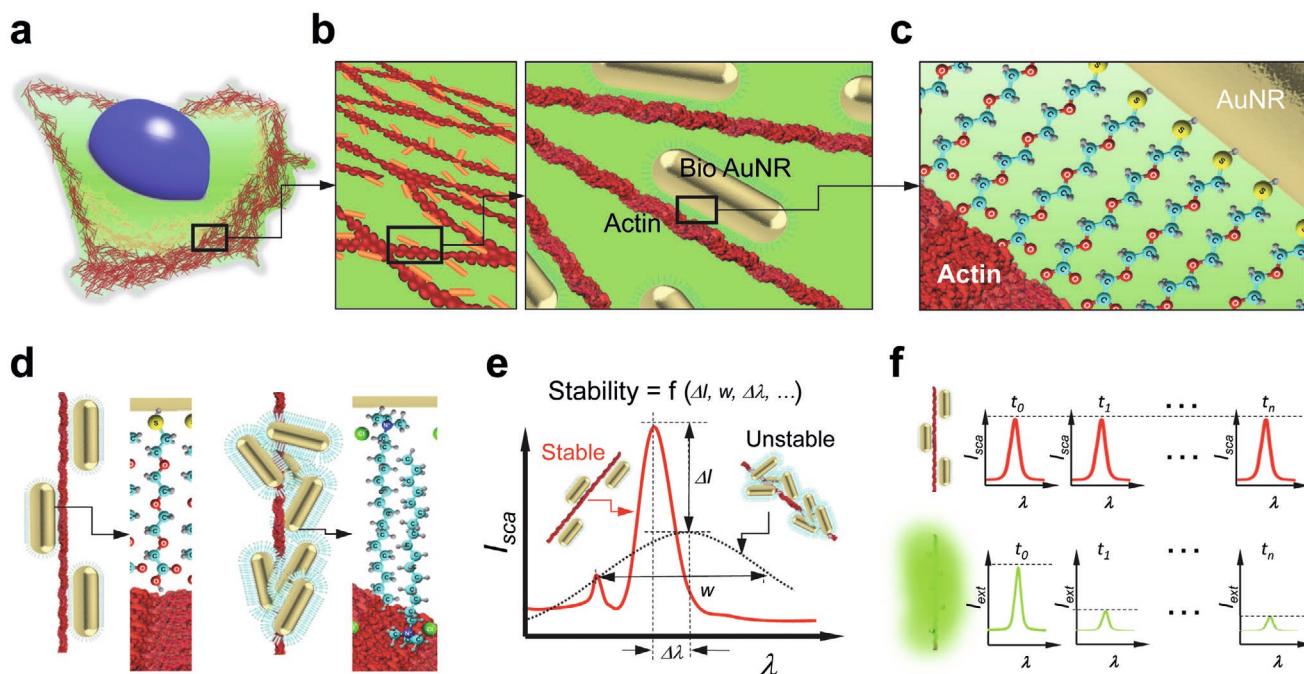


**Figure 1.** Optically and structurally stabilized plasmobio interlinking networks (PBINs). a) Conceptual schematic of cellular interlinking networks. b) Conceptual schematic of bioinspired plasmobio interlinking networks (PBINs). CTA+ free Bio-AuNRs along actin bundles without any structural aggregation. c) Bioinspired interaction between plasmonic nanostructure and interlinking network (e.g., actin). d) CTA+ free Bio-AuNRs assemble along interlinking networks (left), while conventional approaches result in structural instability and aggregation (right). e) Spectral uniformity and sensitivity resulting from the uniform and high-density distribution of CTA+ free Bio-AuNRs. This stability in the optical signal leads to consistent high-resolution imaging on the long-term scale. f) Stable and non-photobleaching signals obtained from PBIN (red line), enabling long term imaging compared with conventional approaches (green line).

Achieving CTA+ free prepares the essential foundation for visualizing dynamic interlinking networks. Traditionally, AuNRs<sup>[14–25]</sup> are synthesized with a strong cationic charge from hexadecyltrimethylammonium bromide (CTAB) capping,<sup>[26–34]</sup> which can impact subsequent ligand exchange.<sup>[35]</sup> In this study, the alternative bromide surfactant, CTAC, was used as the primary surfactant for seed-mediated growth of AuNRs to achieve CTA+ free. The zeta potentials of CTAC–AuNRs and CTAB–AuNRs are 24.7 and 36.1 mV, respectively (Figure S1, Supporting Information). Ligand exchange was conducted by adapting a round trip ligand exchange approach<sup>[17]</sup> for CTAC–AuNRs. To quantitatively assess that AuNRs were indeed CTA+ free, high resolution X-ray photoelectron spectroscopy (XPS) was conducted.

We first investigated the exchange of CTAC with an incoming ligand, in this case, polymer polyethylene glycol (PEG) (Figure 2). Multiple surface washings are necessary to achieve CTA+ free Bio-AuNRs. However, excessive washing also leads to particle aggregation due to the increased particle–particle interactions, which subsequently results in structurally unstable AuNRs. To determine the optimal level of surface washings, we quantified the elemental components of C 1s as a function of the number of surface washings  $n_{sw}$ . At  $n_{sw} = 0$ , we observed a single C–C peak from CTAC. The low elemental concentration of Au 4f indicated it was initially buried by unbound ligands. Ligand exchange followed by a single surface washing ( $n_{sw} = 1$ ) led to a strong C–O–C peak. With more surface washings, the appearance of Au 4f peaks strongly suggested absence of unbound ligands. The O–C=O peak finally

appeared, which is attributed to PEG and indicates successful grafting of functional groups.

To confirm CTA+ free, we measured the elemental concentration of N 1s originating from CTAC (Figure 2). At  $n_{sw} = 0$ , we observed a strong N 1s peak at 399 eV. The N 1s peak then disappeared with surface washings. These results clearly show that CTAC can be completely removed to yield CTA+ free AuNRs. However, unlike the N 1s level, Cl 2p peak was observed even after  $n_{sw} = 20$ , thereby indicating strongly bound chloride. We found the chloride peak was attributed to strongly bound chloride originating from the precursor, not from CTAC. To investigate the origin of the strongly bound chloride, we studied three chloride peaks: C–C peak at 284 eV, C–O–C peak at 285.5 eV, and O–C=O peak at 288.5 eV, which correspond to the alkyl chain of CTAC, PEG chain, and PEG carboxylic functional group, respectively. We observed the level of O–C=O peak, corresponding to the PEG carboxylic functional group, increased as a function of surface washings  $n_{sw}$ . To further confirm the origin of the strongly bound chloride, we also characterized the surface elements of CTAB–AuNRs (Figures S2–S4, Supporting Information). These results also strongly support that the chloride peak is an indicator of strongly bound chloride originating from the precursor. Taken together, these results show that CTAC can be completely removed to yield CTA+ free AuNRs. To the best of our knowledge, all existing ligand exchange protocols focus on the removal of CTAB. In this work, complete ligand exchange of CTAC—indicated by the absence of nitrogen N 1s originating from CTAC—can be achieved to yield CTA+ free

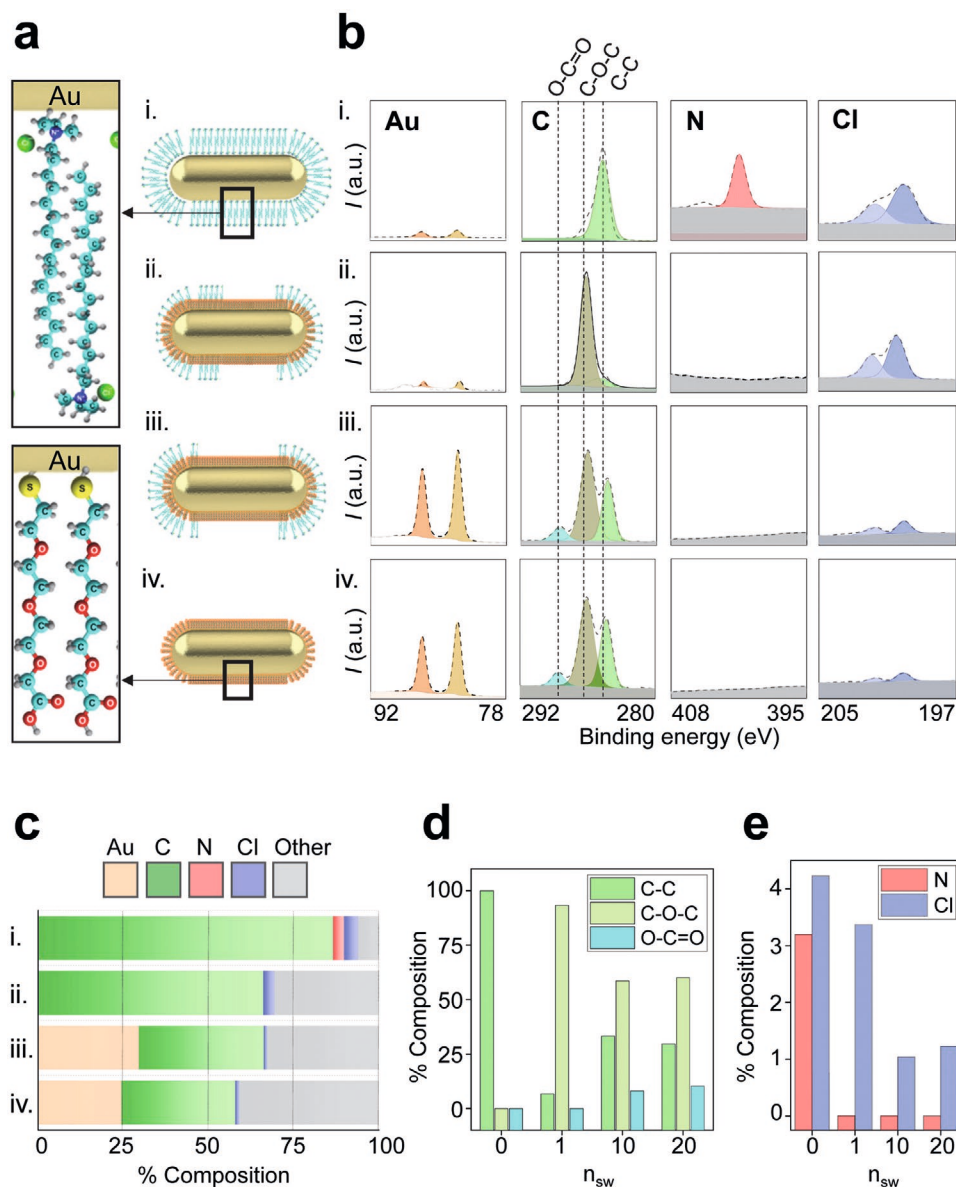


**Figure 2.** CTA+ free Bio-AuNRs are the foundation for stable interlinking networks. a) Conceptual schematic before and after synthesis of CTA+ free Bio-AuNRs. b) Synthetic steps and corresponding XPS spectra to achieve CTA+ free Bio-AuNRs. i)  $n_{sw} = 0$ , ii)  $n_{sw} = 1$ , iii)  $n_{sw} = 10$ , iv)  $n_{sw} = 20$ . c) Quantitative elemental compositions. i)  $n_{sw} = 0$ , ii)  $n_{sw} = 1$ , iii)  $n_{sw} = 10$ , iv)  $n_{sw} = 20$ . d) Quantitative elemental components of C 1s as a function of  $n_{sw}$ . e) Quantitative analysis of N 1s and Cl 2p as a function of  $n_{sw}$ .

gold nanorods, laying the foundation for stable interlinked networks.

For super-resolution applications requiring stability at the nanometer scale, a new method to measure stability is needed. We introduce a new stability algorithm, referred to as the comprehensive stability parameter (CSP), to quantitatively and comprehensively analyze stability (Figure 3). Traditionally, to estimate the stability of plasmonic nanostructures, spectral features, such as the change of the peak extinction rate, shift of the resonant peak, change of the extinction ratio at 400 and 800 nm ( $A_{400}/A_{800}$ ), aggregation index, and ratio of the longitudinal surface plasmon resonance to the transverse surface plasmon resonance, have been used.<sup>[36–39]</sup> However, most approaches rely on only on a single spectral feature and/or a

subset of spectral features, thereby achieving limited results on the overall structural and optical stability of plasmonic nanostructures. Particularly, these limitations have implications on complicated geometries, such as interlinked networks.

Here, the CSP incorporates the entire spectrum to avoid potential bias from a single spectral feature and/or a subset of spectral features. Structurally stable AuNRs exhibit minimal changes of spectral features, while structurally unstable AuNRs yield significant changes of spectral features (Figure 3; Figure S5, Supporting Information). By comparing the cosine similarity between the original and final spectra, the CSP algorithm can obtain a similarity factor to calculate a normalized CSP value from 0 to 1, where higher stability of nanostructures leads to a larger CSP value.

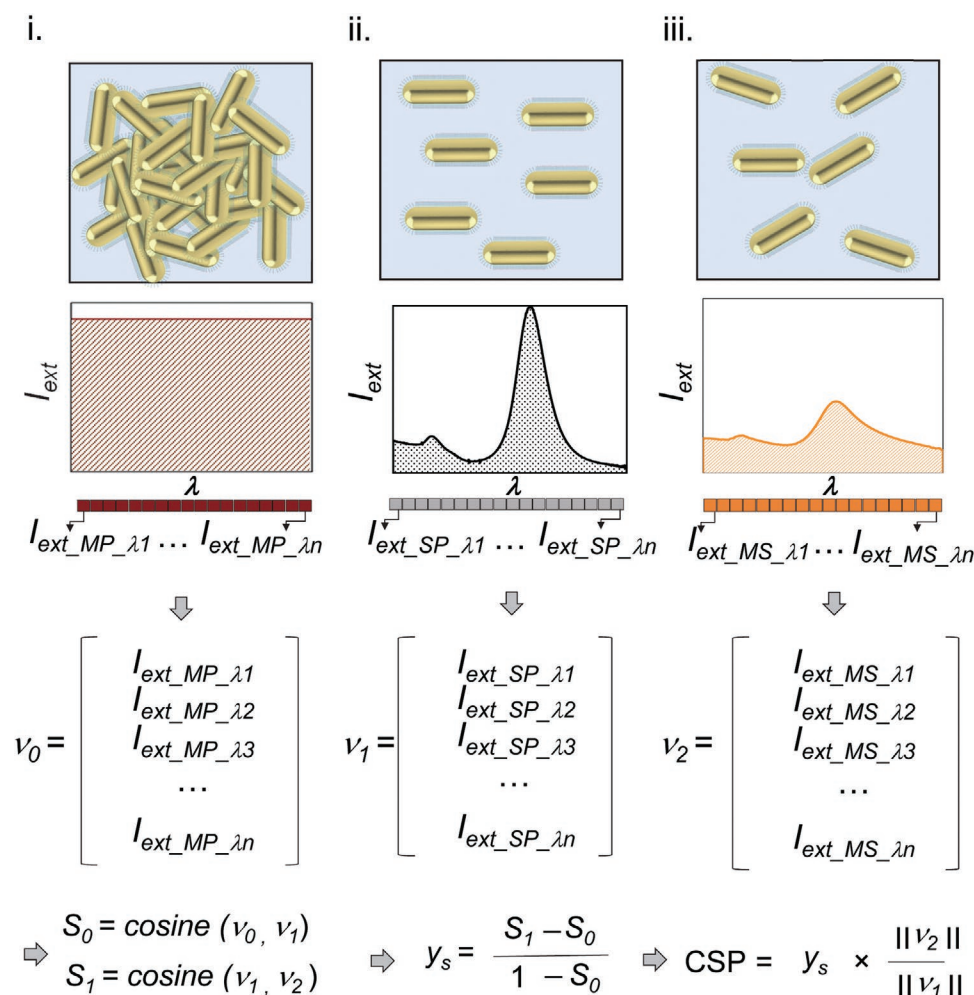


**Figure 3.** Comprehensive stability parameter (CSP) is a new algorithm to quantify stability. After acquiring the spectra of i) highly aggregated, ii) uniformly distributed, and iii) sample AuNRs, respectively, cosine similarities,  $S_0$  and  $S_1$ , are performed between the unstable reference spectrum (brown curve,  $v_0$ ), stable reference spectrum (black curve,  $v_1$ ), and experiment spectrum (orange curve,  $v_2$ ). The relative similarity  $\gamma_s$ , is obtained by calibrating  $S_0$  and  $S_1$  from 0 to 1. Finally, CSP is obtained by multiplying  $\gamma_s$  with the ratio of the vector norms in order to rescale.

The UV-vis spectra of highly dispersed AuNRs (highly stable), fully aggregated AuNRs (highly unstable), and sample AuNRs were acquired and labeled as  $v_0, v_1$ , and  $v_2$ , respectively, after the vectorization and truncation of the spectra. The cosine similarities,  $S_0$  and  $S_1$ , were then calculated between  $v_0$  and  $v_1$  and between  $v_1$  and  $v_2$ , respectively, using the Euclidean dot product formula

$$S_0 = \cos(\theta_0) = \frac{v_1 \cdot v_0}{\|v_1\| \|v_0\|} = \frac{\sum_{i=1}^n v_{1,i} v_{0,i}}{\sqrt{\sum_{i=1}^n v_{1,i}^2} \sqrt{\sum_{i=1}^n v_{0,i}^2}} \quad (1)$$

where  $v_{0,i}$  and  $v_{1,i}$  are the components of vectors  $v_0$  and  $v_1$ . Based on Equation (1), the similarity  $S$  ranges from  $-1$  to  $1$ .  $S = 1$  indicates exactly identical spectra, while  $S = -1$  indicates the opposite sign of the two vectors. To normalize these cosine similarities, a relative similarity  $\gamma_s$  is derived

$$\gamma_s = \frac{S_1 - S_0}{1 - S_0} \quad (2)$$

The value of  $\gamma_s$  is between 0 to 1, where  $\gamma_s = 0$  represents a highly unstable reference while  $\gamma_s = 1$  denotes a highly stable reference. Finally, the CSP is derived by multiplying the relative similarity  $\gamma_s$  with the Euclidean norms of  $v_2$  and  $v_1$

$$\text{CSP} = \gamma_s \times \frac{\|v_2\|}{\|v_1\|} \quad (3)$$

By comprehensively incorporating the entire spectrum, the CSP is able to detect minute instability undetectable using traditional methods. We simulated UV-vis spectra showing varying degree of aggregation (Figure 4a). From the simulated spectra, we then calculated the corresponding CSP as a function of degree of aggregation (Figure 4b). As the peak width ( $w$ ) increased from 110 to  $\approx 400$  nm, the peak intensity at  $\lambda = 750$  nm ( $I_{750\text{nm}}$ ) dropped from 1 to 0.45 due to aggregation. Conventionally, a ratio method is traditionally used based on the ratio  $r$  between the longitudinal peak and the transverse peak. For the ratio method,  $r$  remains constant at  $\approx 0.43$ , thereby suggesting stability. By contrast, the CSP captures changes across the entire spectra. The CSP decreased from 1 to 0.25, thereby

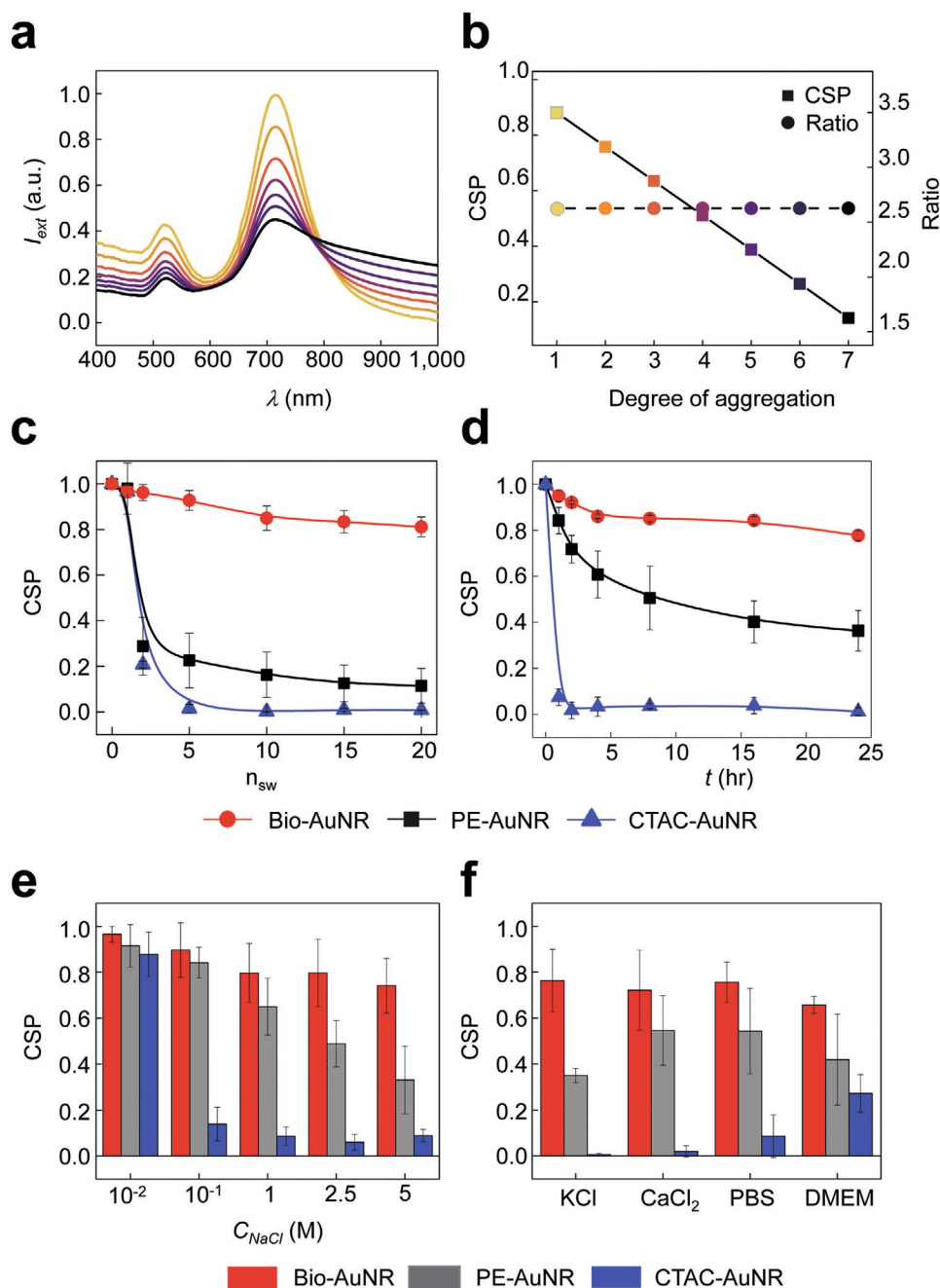


**Figure 4.** CSP is able to detect minute instability undetectable using traditional methods. a) Series of simulated spectra showing varying degree of aggregation from unaggregated (yellow) to aggregated (black). b) Calculated CSP versus traditional ratio method as a function of degree of aggregation corresponding to part a. c) CSP as a function of  $n_{sw}$  comparing CTA+ free Bio-AuNRs, partially exchanged (PE) AuNRs and CTAC-AuNRs. d) CSP as a function of time comparing CTA+ free Bio-AuNRs, PE-AuNRs and CTAC-AuNRs. e) CSP as a function of  $C_{NaCl}$  comparing CTA+ free Bio-AuNRs, PE-AuNRs, and CTAC-AuNRs. f) CSP comparing CTA+ free Bio-AuNRs, PE-AuNRs, and CTAC-AuNRs in various buffers.

capturing gradual, minimal instability not detectable with the conventional ratio method (Figure 4b). Experimental data (Figure S8, Supporting Information) is also in agreement that the conventional ratio method is less sensitive than the CSP.

Using the derived CSP concept, we experimentally evaluated the CSP of prepared CTA+ free Bio-AuNRs by evaluating CSP as a function of  $n_{sw}$  (Figure 4c; Figure S6, Supporting Information). For complete ligand exchange, CTA+ free Bio-AuNRs

can sustain as much as 20 physical surface washings ( $n_{sw} = 20$ ) while maintaining stability in the highly stable zone. By contrast, the CSP of partially exchanged AuNRs was initially semistable and then rapidly decreased, reaching the unstable zone. Further surface washings caused the CSP value to drop to 0.1. CTAC-AuNRs showed CSP = 0 after just  $n_{sw} = 2$ .

We also evaluated the CSP of CTA+ free Bio-AuNRs as a function of ionic strength (Figure 4e; Figure S6, Supporting

Information). In the ion concentration range of 0.01–5.0 M,  $CSP_{Bio-AuNRs}$ ,  $CSP_{PE-AuNRs}$ , and  $CSP_{CTAC-AuNRs}$  decreased from 0.85 to 0.7 (highly stable), 0.8 to 0.3 (unstable), and 0.7 to 0.05 (highly unstable), respectively, indicating CTA+ free Bio-AuNRs maintained stability. Evaluating the CSP of CTA+ free Bio-AuNRs over time,  $CSP_{Bio-AuNRs}$  ranged between 0.8 and 1.0 (stable) in 5 M NaCl solution over 24 h time period (Figure 4d). During the same time period, the CSP of partially exchanged AuNRs ( $CSP_{PE-AuNRs}$ ) decreased from 1.0 to 0.4 and the CSP of CTAC–AuNRs ( $CSP_{CTAC-AuNRs}$ ) dropped to 0.1 (highly unstable). In addition,  $CSP_{Bio-AuNRs}$  ranged between 0.6 and 0.75 in various types of ionic solutions and physiological buffers, including KCl, CaCl<sub>2</sub>, phosphate-buffered solution (PBS), and Dulbecco's modified eagle's medium (DMEM) (Figure 4f). Owing to its stability under various physiological conditions, the incubation of  $1 \times 10^{-9}$  M CTA+ free Bio-AuNRs (Figure S7, Supporting Information) demonstrated >90% cell viability rate, while CTAB–AuNRs demonstrated <10% cell viability rate under the same concentration.

With Bio-AuNRs which are CTA+ free and structurally stable under physical, chemical, and biological environments, we constructed interlinking networks. Here, we constructed PBIN with actin as a model of interlinking networks of the cytoskeleton. We found that efficient crosslinking in PBIN could be achieved with CTA+ free Bio-AuNRs of 0.82 CSP, whereas interlinking networks poorly formed with 0.16 CSP (Figure 5). To quantify the minimum threshold for establishing PBINs, we prepared a series of AuNRs with varying degree of aggregation to crosslink with actin. We then compared the CSP with the crosslinking coefficient ( $Q_{CC}$ ). The CSP quantifies the stability of CTA+ free Bio-AuNRs. The  $Q_{CC}$  quantifies the crosslinking of AuNR-actin networks (Methods section). Comparing the CSP and the  $Q_{CC}$ , we observed that a steep decline of the  $Q_{CC}$  occurred at 0.8 CSP (Figure 5). Thus, we conclude the minimum cutoff for establishing PBINs is 0.8 CSP. Furthermore, we compared the CSP with the conventional ratio method at the minimum cutoff of 0.8 CSP. The conventional ratio method remained relatively constant at the minimum threshold (Figure S8, Supporting Information). In contrast, the CSP sharply decreased, thereby capturing gradual, minimal instability (Figure S8, Supporting Information). We conclude the CSP is more sensitive than the conventional ratio method for analyzing PBINs. Importantly, such sensitivity makes the CSP more reliable for super-resolution applications requiring stability at the nanometer scale.

High crosslinking rate (ratio of AuNRs with high affinity to actin) is necessary for super-resolution imaging. With PBIN exhibiting 97% crosslinking rate (Figure S9, Supporting Information), darkfield microscopy images show CTA+ free Bio-AuNRs uniformly assembled along the network, allowing fine structural features of the network to be clearly visualized. Intensity profiles show several peaks with low background, indicating individual CTA+ free Bio-AuNRs were well separated and a high signal-to-noise ratio can be achieved. Computed electric field distributions confirmed individual plasmonic properties were preserved. By contrast, poor crosslinking resulted in aggregated assemblies where network structural details could not be visualized. Computed electric field distributions showed individual plasmonic properties were lost in the case of poor crosslinking. Large background contributed to the small signal-to-noise ratio

and degraded the imaging quality, impeding super-resolution imaging capabilities.

After establishing structural stability, we studied the optical stability of PBIN (Figure 5). We first compared fluorescent interlinking networks with PBIN. Fluorescent interlinking networks rapidly decreased in intensity from 0.9 to 0.1 within minutes, attributed to photobleaching. By contrast, PBIN was not susceptible to photobleaching and maintained consistent intensity between 0.95 and 0.97 over extended time periods important for capturing dynamics of interlinking networks. Actin is well-known to depolymerize by removing subunits at its polymer ends, and such dynamics gives rise to cytoskeletal reorganization and motility. Whereas many studies have been conducted on the short term dynamics of actin, little is known about the long term dynamic properties of actin depolymerization. This is due in part because of current technological limitations in long term, continuous imaging capabilities. With long the term, continuous capabilities of PBIN, we studied the depolymerization process. PBIN slowly depolymerized over  $\approx 360$  min and disappeared after 450 min. Such long term dynamics cannot be captured in fluorescent interlinking networks. As an active/responsive material, we studied PBIN in response to optical stimulus. We were able to observe  $\approx 200$ –300 nm displacements using remotely controlled, focused  $\lambda = 730$  nm, 9 mW CW laser light. Using on-resonance wavelength (730 nm) and off-resonance resonant wavelength (930 nm), displacements as a function of illumination power were reversible (Figure S10, Supporting Information), showing the potential of PBIN as an active/responsive material.

In conclusion, we demonstrated optically and structurally stable PBIN exhibiting 100% CTA+ free and 97% crosslinking rate. Necessary for structural and optical stability, we introduced a new stability algorithm to comprehensively quantify stability under various physical, chemical, and biological environments. Free from photobleaching, we demonstrated long term imaging of PBIN. This work opens the way for super-resolution imaging of dynamic interlinking networks free of photobleaching. New long term studies of physical ageing and/or photochemical ageing can be conducted toward the design of robust materials. Long term optically responsive functionality can be utilized to develop active materials and devices.

## Experimental Section

**Chemicals and Materials:** CTAC, CTAB, sodium oleate (NaOL), hydrogen tetrachloroaurate (III) trihydrate (HAuCl<sub>4</sub> · 3H<sub>2</sub>O), acetone, calcium chloride (CaCl<sub>2</sub>), 2-propanol (IPA), L-ascorbic acid, potassium chloride (KCl), silver nitrate (AgNO<sub>3</sub>), sodium borohydride (NaBH<sub>4</sub>), hydrochloric acid (HCl), 6-mercaptohexanoic acid (MHA), 1-dodecanethiol (DDT), toluene, methanol, 2-mercaptoethanol, sodium phosphate dibasic (Na<sub>2</sub>HPO<sub>4</sub>), sodium chloride (NaCl), methoxy polyethylene glycol thiol, 4-(2-hydroxyethyl)piperazine-1-ethanesulfonic acid, poly(ethylene glycol) 2-mercaptoethyl ether acetic acid, 2-(N-morpholino)ethanesulfonic acid monohydrate, N-(3-dimethylaminopropyl)-N'-ethylcarbodiimide hydrochloride (EDC), DMEM, PBS, adenosine 5'-triphosphate disodium salt hydrate (ATP), adenosine ATP, Tris(2-varboxyethyl) phosphine HCl (TCEP-HCl Tris), ethylenediaminetetraacetic acid (EDTA), magnesium chloride hexahydrate (MgCl<sub>2</sub> · 6H<sub>2</sub>O), DMEM, N-hydroxysulfosuccinimide sodium salt (Sulfo-NHS), Dulbecco's phosphate buffered saline, G-actin protein, and methylcellulose were purchased from Sigma-Aldrich. Cell Live/Dead viability assay kit and fluorophore-labeled G-actin protein

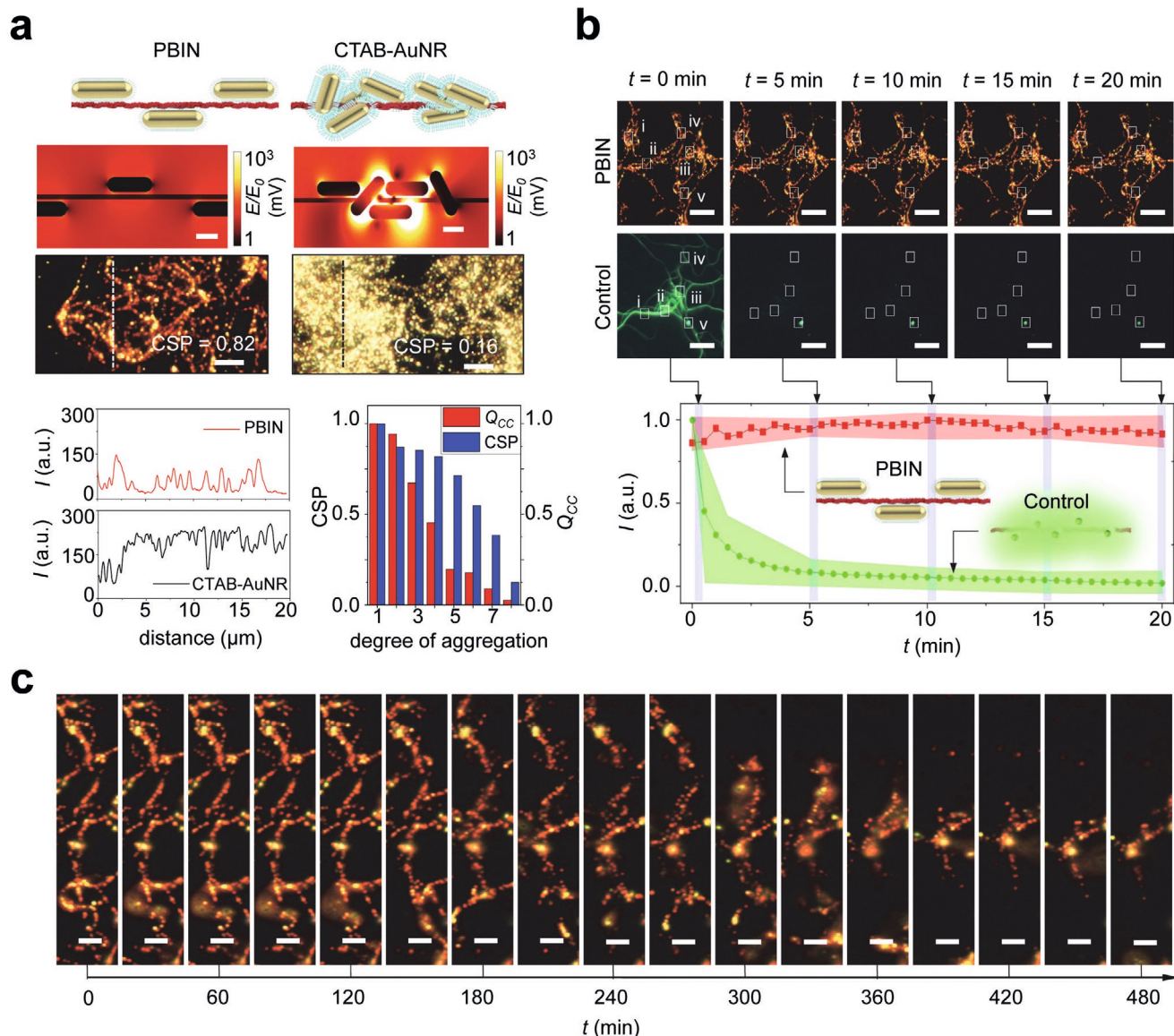


**Figure 5.** Interlinking networks are structurally and optically stable for long term imaging free from photobleaching. a) Conceptual schematics of crosslinking of PBIN constructed with CTAC<sup>+</sup> free BioAuNRs (left) versus CTAC-AuNRs (right). Electric field distribution of PBIN constructed with CTAC<sup>+</sup> free BioAuNRs (left) versus CTAC-AuNRs (right). Scale bar: 35 nm. Darkfield microscopy images of PBIN constructed with CTAC<sup>+</sup> free BioAuNRs (left) versus CTAC-AuNRs (right). Scale bar: 5  $\mu\text{m}$ . Intensity profiles taken along dashed lines in darkfield images for PBIN constructed with CTAC<sup>+</sup> free BioAuNRs versus CTAC-AuNRs. Graph of CSP versus  $Q_{CC}$  as a function of degree of aggregation, where a series of AuNRs with varying degree of aggregation were prepared to crosslink with actin. b) Time course fluorescence images of fluorophore interlinking networks taken over 20 min. In each time course image, locations i-iv are averaged together and plotted on below graph. Time course darkfield images of PBIN taken over 20 min. In each time course image, locations i-iv are averaged together and plotted on below graph. Time course graph comparing scattering intensity (red) versus fluorescence intensity of control (green) corresponding to time course images. c) Long term darkfield imaging of PBIN dynamics over 480 min. Scale bar: 5  $\mu\text{m}$ .

were purchased from Thermo Fisher Scientific. Deionized (DI) water with resistivity 18.2 M $\Omega$  was used.

**Synthesis of CTAC<sup>+</sup> Free Bio-AuNRs:** CTAC-AuNRs were synthesized by bromide-free seed-mediated growth as previously described.<sup>[40]</sup> The dimension of AuNRs was confirmed using scanning electron microscopy. Then, a round-trip phase transfer method<sup>[17]</sup> was adapted to replace CTAC with PEG. Unlike the traditional method focusing on CTAB-AuNRs, process parameters: temperature, centrifugal steps, and incubation time for CTAC-AuNRs were modified (see details in the Supporting Information).

**Zeta Potential Analysis:** Zeta potential measurements were performed by using a Malvern Zetasizer Nano-ZS. Before measuring, the samples were purified by three rounds of centrifugation at 7000 rpm for 5 min followed by redispersion in DI water to reach a final AuNRs concentration of about O.D. = 10.0 at the longitudinal localized surface plasmon resonance peak.

**XPS Measurement and Data Analysis:** Drop cast deposition of samples was conducted on carefully washed silicon substrates. XPS analyses were conducted with illumination beam of monochromatic Al X-rays at 14 kV and 12 mA. Wide survey spectra were taken from 0 to 600 with

1 eV scan step size, 60 s sweep time with analyzer at 160 eV pass energy and averaged by two times of sweeping to remove the noise. The survey spectra were then calibrated with Au 4f<sub>7/2</sub> at 84.00 eV.

**Comprehensive Stability Parameter:** To conduct CSP analysis, UV-vis spectra of standard aggregated AuNRs (highly unstable), fully dispersed AuNRs (highly stable), and samples were acquired. Using a developed in-house code, all the processes of vectorization and truncation of data, derivation of the cosine similarity, and final normalization steps were performed.

**Crosslinking Coefficient:** Crosslinking coefficient is a parameter to quantify the quality of AuNR-actin crosslinked networks.

$$Q_{CC} = \kappa_n \eta_{cc} \frac{\sqrt{S_{ntwrk}}}{STD(I_{pks})} U_1 \quad (4)$$

where  $\kappa_n$  is the normalization factor,  $\eta_{cc}$  is associated with the ratio of AuNRs which can be crosslinked to the actin network to the total number of AuNRs.  $\sqrt{S_{ntwrk}}$  is the relative size of the actin network and equal to the number of AuNRs on the actin network times the relative average area of one AuNR.  $STD(I_{pks})$  is the standard deviation of the intensity of peaks.  $U_1$  is a uniformity parameter which focuses on the intensity of pixels within a certain range.  $U_1 = \frac{1}{m} \left\| \frac{I_X}{a_{ref}} \right\|$ , where

$I_X = \{ |I| > \max\{\min\{\max\{I, column\}\} \cup \min\{\max\{I, row\}\}\} \cap I < a_{agg}\}$ .  $m$  is the number of elements in  $I_X$ .  $a_{ref}$  is the average intensity of colloidal AuNRs under the same imaging setup.  $a_{agg}$  is a factor related to the predefined intensity threshold of aggregated AuNRs.

**Structural Stability of CTA+ Free Bio-AuNRs:** To investigate particle aggregation related to structural stability, repeated washing steps of the CTA+ free Bio-AuNRs were performed. At each washing step, after centrifugation 5000 rpm for 5 min, the supernatants were removed and CTA+ free Bio-AuNRs were resuspended by adding the same amount of DI water. Washing steps were repeated 20 times. As a function of washing steps, UV-vis spectra of CTA+ free Bio-AuNRs were acquired using a spectrometer (Agilent Cary 3500 UV-vis spectrophotometer). At each washing step, CSP values were obtained. To achieve statistical confidence, these tests were repeated three times.

**Chemical and Biological Stability of CTA+ Free Bio-AuNRs:** We prepared NaCl (0.01 to 5 M), CaCl<sub>2</sub> (5 M), KCl (3 M), PBS, and DMEM solutions. We then centrifuged at 5000 rpm for 5 min, removed the supernatant, and added the prepared ion solution in the tube containing CTA+ free Bio-AuNRs. We acquired UV-Vis spectra using a spectrometer (Agilent Cary 3500 UV-VIS spectrophotometer). At each washing step, we obtained CSP values. To achieve statistical confidence, we performed these tests three times.

**Construction of PBIN:** Working solutions of labeled and unlabeled G-actin protein at 1 mg mL<sup>-1</sup> (200 × 10<sup>-6</sup> M ATP at pH 7.0, 500 × 10<sup>-6</sup> M TCEP at pH 7, 0.1 × 10<sup>-3</sup> M CaCl<sub>2</sub>) were prepared. The labeled and unlabeled G-actin protein was polymerized in 10× KMEI (KCl, MgCl<sub>2</sub>, EDTA, Imidazole). EDC/NHS bioconjugation chemistry was next employed to form NH<sub>2</sub><sup>+</sup> group on the Bio-AuNRs. To obtain the final PBIN, the functionalized Bio-AuNRs and the polymerized actin sample were crosslinked by mixing them at a 1:1 volume ratio and incubating for 1 h. After the crosslinking step, the sample was washed gently to remove non-crosslinked particles by dropping and withdrawing DI water from the PBIN five times.

**Darkfield and Fluorescence Imaging:** For the imaging, PBIN (100 μL) with G-actin was incubated in a petri dish for 30 min. Then, the treated G-actin was washed three times with 1× PBS, and the G-actin was then placed into a PDMS microchamber on a microscope slide. To acquire scattering signals and images, a microscopy system consisted of an inverted microscope (Olympus IX73) equipped with a darkfield condenser (1.2–1.4 numerical aperture) and a white light source (Xenon Arc Lamp). Then, darkfield images of treated G-actin were acquired using a digital camera (Q-color3, Olympus). The scattering spectra from the probes at different positions were collected using a monochromator (300 mm focal length and 300 grooves per mm, Acton Research) with a cooled spectrograph CCD camera (Roper Scientific). A 2 μm wide aperture was placed in front of the monochromator to keep only a single probe in the region-of-interest.

**Electromagnetic Field Calculation:** The Helmholtz wave equation ( $\nabla \times (\mu_r^{-1} \nabla \times E) - k_0^2 (\epsilon_r - j\sigma\omega\epsilon_0) E = 0$ ) was solved to estimate near-field electromagnetic radiation around a plasmonic structure with a finite element analysis method (COMSOL Multiphysics software). Hybrid mesh structures to adopt its round and sharp geometry of PBIN were introduced. It was assumed that relative permeability ( $\mu_r$ ) and complex permittivity ( $\epsilon_r$ ) of Au were  $\mu_r = 1$  and  $\epsilon_r = f(\lambda)$ , respectively. In the simulation, the polarization vector was applied in the direction parallel to the PBIN structure, whereas the direction of the  $k$ -vector was taken to be perpendicular to the plane of the structure. Regarding outer boundary, perfect absorption was used to minimize spurious reflections by setting a perfectly matched layer and an integration layer in the concentric space. The dimensions of the PBIN (AuNR; longitudinal length = 60 nm and transverse diameter ( $d_{in}$ ) = 30 nm, and Actin; 8 nm) were chosen based on the acquired images.

## Supporting Information

Supporting Information is available from the Wiley Online Library or from the author.

## Acknowledgements

W.-K.L. and G.C. contributed equally to this work. This work was supported by the Air Force Office of Scientific Research (AFOSR FA9550-16-1-0272 and FA9550-19-1-0186), National Science Foundation (NSF ECCS 1454188), and academic research fund at the University of Michigan.

## Conflict of Interest

The authors declare no conflict of interest.

## Keywords

actin, plasmonic nanostructures, responsive materials, subdiffraction, super-resolution

Received: August 3, 2020  
Revised: September 24, 2020  
Published online: December 2, 2020

- [1] T. Dvir, B. P. Timko, D. S. Kohane, R. Langer, *Nat. Nanotechnol.* **2011**, *6*, 13.
- [2] K. Baranes, M. Shevach, O. Shefi, T. Dvir, *Nano Lett.* **2016**, *16*, 2916.
- [3] X. Yang, J. Yang, L. Wang, B. Ran, Y. Jia, L. Zhang, G. Yang, H. Shao, X. Jiang, *ACS Nano* **2017**, *11*, 5737.
- [4] A. K. Gaharwar, I. Singh, A. Khademhosseini, *Nat. Rev. Mater.* **2020**, *5*, 686.
- [5] B. A. Evans, A. R. Shields, R. L. Carroll, S. Washburn, M. R. Falvo, R. Superfine, *Nano Lett.* **2007**, *7*, 1428.
- [6] Y. Liu, Y. Park, S. E. Lee, *Appl. Phys. Lett.* **2016**, *109*, 013109.
- [7] T. A. Klar, S. W. Hell, *Opt. Lett.* **1999**, *24*, 954.
- [8] S. W. Hell, M. Kroug, *Appl. Phys. B* **1995**, *60*, 495.
- [9] M. Hofmann, C. Eggeling, S. Jakobs, S. W. Hell, *Proc. Natl. Acad. Sci. U.S.A.* **2005**, *102*, 17565.
- [10] T. Dertinger, R. Colyer, G. Iyer, S. Weiss, J. Enderlein, *Proc. Natl. Acad. Sci. U.S.A.* **2009**, *106*, 22287.

- [11] P. Lemmer, M. Gunkel, D. Baddeley, R. Kaufmann, A. Urich, Y. Weiland, J. Reymann, P. Müller, M. Hausmann, C. Cremer, *Appl. Phys. B* **2008**, 93, 1.
- [12] E. Betzig, G. H. Patterson, R. Sougrat, O. W. Lindwasser, S. Olenych, J. S. Bonifacino, M. W. Davidson, J. Lippincott-Schwartz, H. F. Hess, *Science* **2006**, 313, 1642.
- [13] M. J. Rust, M. Bates, X. Zhuang, *Nat. Methods* **2006**, 3, 793.
- [14] B. Nikoobakht, M. A. El-Sayed, *Chem. Mater.* **2003**, 15, 1957.
- [15] L. Gou, C. J. Murphy, *Chem. Mater.* **2005**, 17, 3668.
- [16] V. Baumann, P. J. Friedrich Röttgermann, F. Haase, K. Szendrei, P. Dey, K. Lyons, R. Wyrwich, M. Gräßel, J. Stehr, L. Ullerich, F. Bürsgens, J. Rodríguez-Fernández, *RSC Adv.* **2016**, 6, 103724.
- [17] A. Wijaya, K. Hamad-Schifferli, *Langmuir* **2008**, 24, 9966.
- [18] H. Takahashi, Y. Niidome, T. Niidome, K. Kaneko, H. Kawasaki, S. Yamada, *Langmuir* **2006**, 22, 2.
- [19] H. Nakashima, K. Furukawa, Y. Kashimura, K. Torimitsu, *Langmuir* **2008**, 24, 5654.
- [20] X. Li, J. Qian, S. He, *Nanotechnology* **2008**, 19, 355501.
- [21] A. Gole, C. J. Murphy, *Chem. Mater.* **2005**, 17, 1325.
- [22] T. S. Hauck, A. A. Ghazani, W. C. W. Chan, *Small* **2008**, 4, 153.
- [23] S. Zalipsky, *Adv. Drug Delivery Rev.* **1995**, 16, 157.
- [24] S. E. Lee, G. L. Liu, F. Kim, L. P. Lee, *Nano Lett.* **2009**, 9, 562.
- [25] S. E. Lee, D. Y. Sasaki, Y. Park, R. Xu, J. S. Brennan, M. J. Bissell, L. P. Lee, *ACS Nano* **2012**, 6, 7770.
- [26] G. González-Rubio, V. Kumar, P. Llombart, P. Díaz-Núñez, E. Bladt, T. Altantzis, S. Bals, O. Peña-Rodríguez, E. G. Noya, L. G. MacDowell, A. Guerrero-Martínez, L. M. Liz-Marzán, *ACS Nano* **2019**, 13, 4424.
- [27] C. Kinnear, H. Dietsch, M. J. D. Clift, C. Endes, B. Rothen-Rutishauser, A. Petri-Fink, *Angew. Chem., Int. Ed.* **2013**, 52, 1934.
- [28] J. Conde, J. T. Dias, V. Grazú, M. Moros, P. V. Baptista, J. M. de la Fuente, *Front. Chem.* **2014**, 2, 1.
- [29] S. E. Lee, D. Y. Sasaki, T. D. Perroud, D. Yoo, K. D. Patel, L. P. Lee, *J. Am. Chem. Soc.* **2009**, 131, 14066.
- [30] X. C. Jiang, A. Brioude, M. P. Pileni, *Colloids Surf., A* **2006**, 277, 201.
- [31] T. K. Sau, C. J. Murphy, *Langmuir* **2004**, 20, 6414.
- [32] W. Ni, X. Kou, Z. Yang, J. Wang, *ACS Nano* **2008**, 2, 677.
- [33] I. C. Pekcevik, L. C. H. Poon, M. C. P. Wang, B. D. Gates, *Anal. Chem.* **2013**, 85, 9960.
- [34] D. Shi, C. Song, Q. Jiang, Z. G. Wang, B. Ding, *Chem. Commun.* **2013**, 49, 2533.
- [35] A. S. D. S. Indrasekara, R. C. Wadams, L. Fabris, *Part. Part. Syst. Charact.* **2014**, 31, 819.
- [36] M. Sethi, G. Joung, M. R. Knecht, *Langmuir* **2009**, 25, 317.
- [37] H. de Puig, S. Federici, S. H. Baxamusa, P. Bergese, K. Hamad-Schifferli, *Small* **2011**, 7, 2477.
- [38] J. C. Y. Kah, A. Zubieta, R. A. Saavedra, K. Hamad-Schifferli, *Langmuir* **2012**, 28, 8834.
- [39] X. Du, W.-C. Lin, Q. Shou, X. Liang, H. Liu, *Colloid Polym. Sci.* **2019**, 297, 891.
- [40] X. Ye, Y. Gao, J. Chen, D. C. Reifsnnyder, C. Zheng, C. B. Murray, *Nano Lett.* **2013**, 13, 2163.